 FDMP, vol.2, no.1, pp.27-45, 2006

Effect of Bubble Size and Location on Segregation Pattern and Interface Shape in Microgravity Crystal Growth

M. Kassemi[1], Y. Wang[2], S. Barsi[1,3] and B.T.F. Chung[2]

Abstract: Microgravity experiments, especially materials processing experiments, have often been hampered by presence of unwanted bubbles. In this work, the effect of thermocapillary convection generated by a bubble on the Bridgman growth of a dilute binary alloy in microgravity is investigated numerically. The model is based on the quasi-steady Navier-Stokes equations for the fluid flow in the melt coupled with the conservation equations for transport of energy and species in the growth ampoule. Numerical results indicate three different growth regimes based on the distance between the bubble and the growth interface: a diffusion dominated regime that is separated from a well-mixed convection dominated regime by a transitionary region where both diffusion and bubble generated convection play an important role. In this transitionary region, the effects of bubble size and bubble location on the interface shape and the radial segregation patterns at the growth front are significant.

Nomenclature

C	Concentration
Ca	Capillary Number, $\frac{\mu U_o}{\gamma}$
c_p	Specific Heat
D	Mass Diffusivity
F_b	Dimensionless Body Force, $\frac{\rho_l g R^2}{V_o \mu}$
$\vec{g}$	Gravity Vector
Gr	Grashof Number, $\frac{g\beta\Delta T R^3}{\nu^2}$
H	Mean Curvature, $\frac{1}{2}(\frac{1}{R_1}+\frac{1}{R_2})$
k	Thermal Conductivity
l	The Distance between the Bubble and the Growth Interface
Ma_T	Thermal Marangoni Number, $Re \cdot \Pr$
Ma_S	Solutal Marangoni Number, $Re \cdot Sc$
$\vec{n}$	Normal Vector
P	Pressure
Pr	Prandtl Number, $\frac{\nu}{\alpha}$
r	Radial Direction Coordinate
R	Bubble Radius, Residual
R'	Dimensionless Radius
S	Solution Vector
Sc	Schmidt Number, $\frac{\nu}{D}$
St	Stefan Number, $\frac{c_{pl}\Delta T}{L}$
$\vec{t}$	Tangential Vector
T	Temperature
V_o	Characteristic Velocity, $\frac{\left\|\frac{d\gamma}{dT}\right\|(\nabla T_\infty)R}{\mu}$
$\vec{V}$	Velocity vector
We	Weber Number, $Re \cdot Ca$

Greek Symbols

α	Thermal Diffusivity
β	Thermal Volume Expansion Coefficient
γ	Surface Tension
θ	Dimensionless Temperature
κ	Partition Coefficient
μ	Dynamic Viscosity
ν	Kinematic Viscosity
ρ	Density
σ	Viscous Stress Tensor
δ	Free Surface Deflection
ε	Convergence Criterion

Subscripts

a	Ampoule
c	Cold
g	Growth
h	Hot
l	Liquid
m	Growth Interface

[1] National Center for Space Exploration Research, NASA Glenn Research Center, Cleveland, OH 44135, U.S.A. Tel: (216)433-5031; Fax: (216)433-5033, Email: Mohammad.Kassemi@grc.nasa.gov

[2] Dept. of Mechanical Engineering, University of Akron, Akron, OH, U.S.A

[3] Dept. of Mechanical Engineering, Case Western Reserve University, Cleveland, OH, U.S.A

n	Normal
o	Reference Quantity
s	Solid
S	Solutal
T	Thermal
top	Top
w	Ampoule wall
∞	Reference Conditions
i	Iteration number
crit	Critical value

1 Introduction

The utility and versatility of semiconducting devices is largely due to the ability of altering the properties of the crystalline material to meet a specific technological need through addition of dopants during the growth process. The performance of the final semiconductor is usually directly dependent on the uniformity of the dopant in the grown crystal [Brown (1988)]. Compositional non-uniformities can make it difficult to achieve certain desirable physical properties in the bulk material [Carruthers (1977)] and can limit reproducibility of the wafer properties. Dopant transport in the melt of the growing crystal is seen to be largely responsible for the compositional inhomogeneities.

Assuming a planar growth interface, Tiller et al. (1953) derived an equation describing the solute distribution, or segregation, in the melt region of a directionally solidifying crystal during a diffusion dominated growth process. Their results indicated that, after neglecting an initial and final transient, a significant portion of the solid crystal is at a uniform composition. Coriell and Sekerka (1979) extended this by showing that even in the diffusion controlled growth, a non-planar growth front can lead to significant levels of solute segregation. Studying growth processes that were not diffusion-controlled, Burton et al. (1953) and Wagner (1954) showed that convection in the melt region will drastically affect the uniformity of solutal concentration in the solid.

Of course, convection in the melt does not only affect solutal transport directly, but also indirectly, as it often also impacts the heat transport in the crucible. This may alter the interface shape which can again, in turn, affect the segregation patterns in the melt. Unfortunately, controlling the levels of convection in the melt region is a difficult task. In many cases this is because natural convection, driven by buoyancy forces resulting from thermally and/or solutally generated density variations in the bulk of the melt, is difficult to avoid and can strongly affect the transport conditions. Significant levels of convection during the crystal growth process are encountered even when a crystal is grown in a thermally stable Bridgman configuration [Crouch et al. (1982), Lehoczky and Szofran (1982)]. These natural convective flows are often due to small, but unavoidable radial temperature or solutal gradients in the melt, caused by a mismatch in thermal conductivities of the solid, melt and ampoule, the interface shape, and the often complex heat transfer linkage between the crucible and the furnace.

One way to eliminate the undesirable effects of natural convection is to carry out the crystal growth operation in the weightlessness environment provided by orbiting spacecraft. Unfortunately, in the microgravity environment, other problems or phenomena that are often masked by the strong buoyancy force on Earth can become prominent (see, e.g., Esmaeeli, 2005; Lappa, 2005a, 2005b). One such phenomenon, especially in solidification experiments, is the effect of bubbles in the melt during the growth process.

Microgravity materials processing experiments are often compromised by the evolution of unwanted bubbles in the liquid. Although these bubbles are highly undesirable, there is currently no effective means of preventing their formation or eliminating their adverse effects. Formation of bubbles has caused problems in microgravity experiments for a long time. Even in the early Skylab mission an unexpectedly large number of bubbles were detected in the four materials processing experiments reported by Papazian and Wilcox (1978). They demonstrated that while during ground-based tests bubbles were seen to detach from the interface easily and float to the top of the melt, in low-gravity tests no detachment from the interface occurred and large bubbles were grown in the crystal.

More recently, the lead-tin-telluride crystal growth experiment of Fripp et al. (1997) flown aboard the USMP-3 mission has provided very interesting results. The purpose of the study was to investigate the effect of natural convection on the solidification process by growing the samples at different orientations with respect to the gravitational field. Large pores and bubbles were found in the three solid crystal samples processed in space. Post-growth characterization of the compositional profiles of the cells indicated considerable levels of mix-

ing even in the sample grown in the hot-on-top stable configuration. The mixing was attributed to thermocapillary convection generated along the surface of these bubbles. Since thermocapillary convection is orientation-independent, diffusion-controlled growth was not possible in any of the samples, even in the top-heated one.

Another microgravity experiment which has reported significant evolution of bubbles in the melt is the dopant segregation study of Matthiesen and co-workers (1993), which involved solidification of selenium-doped GaAs in microgravity during the USML-1 mission. The experiment was designed to investigate the effects of the microgravity environment, the translation rate, and the furnace thermal profile on the axial and radial dopant distributions. Two samples were solidified, both of which contained a considerable number of bubbles. Both samples also exhibited concentrations which were more uniform than expected, especially in the region right below the bubbles. Moreover, post-growth measurements of the selenium dopant concentration in the sample indicated a behavior which could not be easily deciphered. This again suggested the possibility that the diffusion-controlled growth conditions were disrupted by vigorous mixing attributed to surface tension- driven convection generated by the bubbles.

Bubbles were also present in the microgravity Al-In alloy solidification experiment carried out by Andrews et al. (1997) which flew aboard the LMS mission in the summer of 1996. The goal of the microgravity research was to control growth conditions in the absence of buoyancy-driven convection. In order to promote stable interfacial conditions a steep thermal gradient of 100^{o}C/cm was required in the sample. All three processed samples contained a considerable number of bubbles, which were attributed to sticking pistons and entrapped gases liberated during the process. Since it was not possible to control the temperature gradient in the samples effectively, the gradients in all three samples were considerably lower than necessary to promote interface stability. Once again, there was incredible difficulty in interpreting the results of this experiment.

Unlike natural convection, that is driven by density differences generated by either temperature or concentration gradients in the bulk of the melt, bubble-generated Marangoni convection is driven by surface tension forces brought about by temperature or concentration gradients (thermocapillary and solutocapillary convection, respectively) along the free surfaces of the bubble. On earth, the volumetric forces are dominant, especially in apparatuses with large volume to surface ratio. But in the reduced gravity environment of orbiting spacecraft, surface forces become more important. As a result, the bubble-generated Marangoni convection can easily alter the flow, temperature and concentration fields in the melt. Naturally, if these effects are strong enough to extend to the solidification front, they can change interfacial concentration and temperature gradients and lead to unexpected growth conditions.

There have also been two experiments that have directly investigated thermocapillary convection generated by bubbles in reduced gravity using silicone oil as a model fluid. The first microgravity experiment was undertaken by Naumann (1995) and flew on the USML-1 mission in 1992. The second is the reduced gravity experiments of Wozniak et al. (1996), aboard the European TEXUS 33 sounding rocket. The results of these experiments indicate that flows induced by thermocapillary convection can be at least three orders of magnitude larger than the buoyancy-driven convective flows caused by residual acceleration. The aforementioned studies, however, both involve model fluids without any phase change. Therefore, they do not directly address the impact of bubble-generated thermocapillary convection on alloy solidification in microgravity.

These results are all consistent with experimental and computational studies of thermocapillary convection generated by a bubble on a heated surface performed by Kassemi and Rashidnia [1997a,1997b,1998, 2000] where it is numerically and experimentally shown that the thermocapillary flow generated by a bubble can drastically modify the temperature field through vigorous mixing of the fluid around it, especially under microgravity conditions.

Furthermore, in two subsequent papers, Kassemi et al. (2001a, 2001b) showed how a typical microgravity crystal growth process can be affected by thermocapillary convection. Their results indicated that bubble-generated convection can have a significant impact on interfacial segregation patterns especially if the bubble is located close the growth interface. In these studies [Kassemi et al. (2001a), Kassemi et al. (2001b)] attention was focused on the melt region alone by assuming a fixed interface shape that was extracted from the results of a previous space experiment [Matthiesen and Majewski (1993)].

In this present paper, the model encompasses both the solid and the melt regions during the microgravity solidification of a dilute binary alloy. Attention is focused on the effect of bubble size on the segregation patterns in the melt and on the interface shape of the growing crystal. The reader is also cautioned that in the sections that follow we sometimes use the terms *bubble* and *void* interchangeably. We also refer to the interface between the bubble and the melt as the *bubble interface* and the interface between the melt and the solid crystal as the *growth interface*. However, whenever the term interface is mentioned without a specific attribute, it should be understood that it refers to the growth interface.

2 Mathematical Formulation

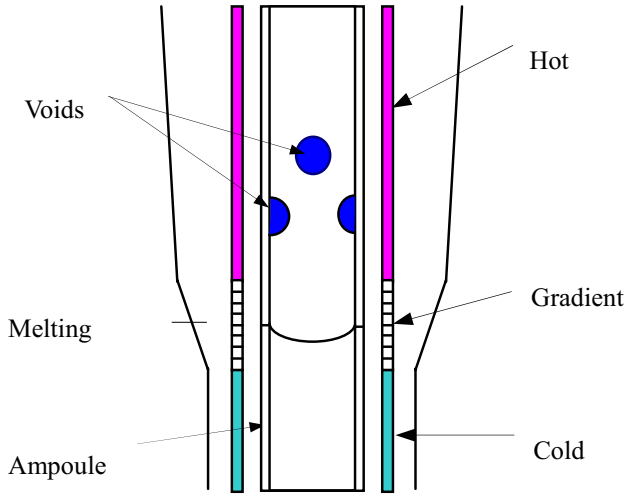

Figure 1 : Schematic of the Growth Configuration.

Microgravity solidification of a single crystal from a dilute binary melt (in this case, selenium-doped gallium arsenide) in a vertical Bridgman furnace is considered. The configuration of the system is depicted in Fig. 1. The ampoule is placed in a three-zone furnace: a cold zone that is isothermal, a gradient zone with a steep temperature gradient and a hot zone with a shallow temperature gradient, *dT/dz*. Directional solidification takes place as the ampoule is pulled through the furnace at a constant pulling rate. Due to the existence of a bubble in the melt (see Fig. 2), surface tension forces created by the temperature gradient along the melt-bubble interface drives a strong thermocapillary flow. In the microgravity environment, the effects of natural convection are negligible; therefore, the bubble-generated thermocapillary convection becomes the main driver for the flow. This recirculating flow disrupts the diffusion-dominated thermal and solutal stratification in the ampoule, resulting in significant alteration of the temperature and concentration profiles near the solid-liquid interface.

2.1 Governing Transport Equations

Since the crystal pulling velocity is quite small and assumed to be equal to the crystal growth rate, a pseudo-steady-state approach is adopted according to which the translation of the ampoule is modeled by the melt entering at the hot end at a uniform growth velocity, V_g and a uniform composition C_0, and the crystal is removed from the cold end at a speed rate that conserves the total mass of the alloy in the system. The GaAs melt is treated as an incompressible Newtonian fluid. All solid and fluid properties except surface tension and fluid density are assumed to be constant. The solidification process can be described mathematically in terms of the mass, momentum, energy and species equations.

The governing equations are cast into a dimensionless form using the following scales. The bubble radius, R, is taken as the characteristic length scale. Pressure is scaled by ρV_o^2; The dimensionless temperature is defined as

$$\theta = \frac{T - T_c}{T_h - T_c} \quad ;$$

Following, the recommendation of Ostrach (1982), the characteristic velocity due to the thermocapillary force is given by:

$$V_o = \frac{\left|\frac{d\gamma}{dT}\right| (\nabla T) R}{\mu} \quad .$$

Concentration is scaled by C_0 at the hot end.

The resulting dimensionless momentum and conservation equations and their respective boundary conditions are given below with the over-bars denoting the dimensionless variables:

In the liquid:

$$\nabla \cdot \overline{V}_l = 0 \tag{1}$$

$$\overline{V}_l \cdot \nabla \overline{V}_l = -\nabla \overline{P} + \frac{1}{Re} \nabla^2 \overline{V}_l - \frac{Gr}{Re^2} (\theta_l - \theta_m) + \frac{F_b}{Re} \tag{2}$$

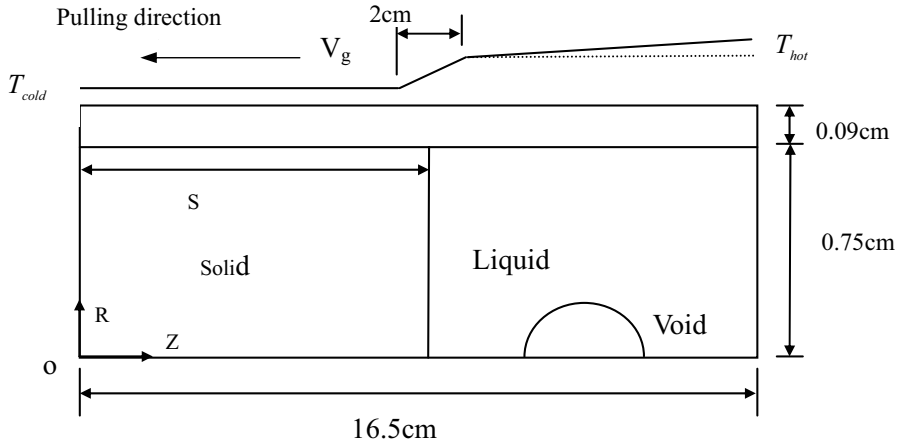

(a)

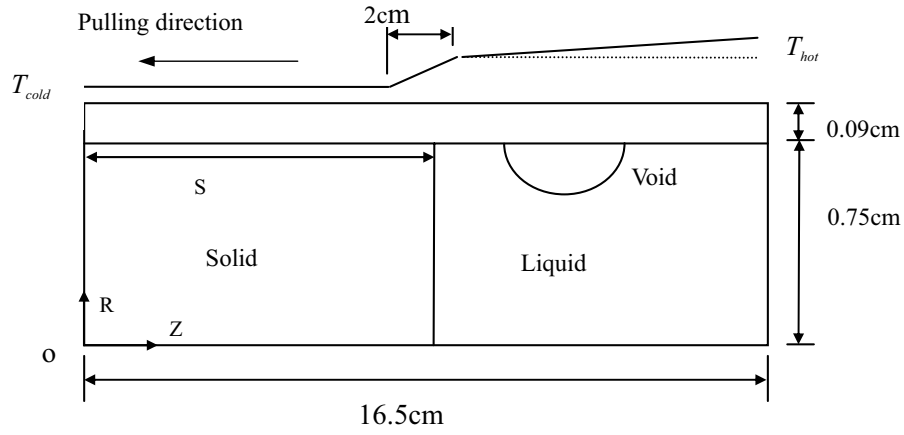

(b)

Figure 2 : Schematic Diagram and Geometric Definitions for (a) the Bubble-in-Center Configuration; (b) the Bubble-on-Wall Configuration.

$$\overline{V}_l \cdot \nabla\theta_l = \frac{1}{Ma_T}\nabla^2\theta_l \tag{3}$$

$$\overline{V}_l \cdot \nabla\overline{C}_l = \frac{1}{Ma_S}\nabla^2\overline{C}_l \tag{4}$$

In the solid, the energy and species equations are:

$$\frac{\rho_s}{\rho_l}\frac{c_{ps}}{c_{pl}}(\overline{V}_s \cdot \nabla\theta_s) = \frac{k_s}{k_l}\frac{1}{Ma_T}\nabla^2\theta_s \tag{5}$$

$$\overline{V}_s \cdot \nabla\overline{C}_s = \frac{D_s}{D_l}\frac{1}{Ma_S}\nabla^2\overline{C}_s \tag{6}$$

In the ampoule walls, the energy equation is:

$$\frac{\rho_w}{\rho_l}\frac{c_{pw}}{c_{pl}}(\overline{V}_w \cdot \nabla\theta_w) = \frac{k_w}{k_l}\frac{1}{Ma_T}\nabla^2\theta_w \tag{7}$$

The associated boundary conditions are as follows:
On the top wall, i.e. $\overline{z} = L/R$:

$$\overline{V}_H = \overline{V}_l\big|_{\overline{z}=L/R} = \frac{\vec{V}_g}{V_0} \tag{8}$$

$$\theta_H = \theta_l\big|_{\overline{z}=L/R} = 1 \tag{9}$$

$$\overline{C}_H = \overline{C}_l\big|_{\overline{z}=L/R} = 1 \tag{10}$$

On the bottom wall, or $\overline{z} = 0$:

$$\overline{V}_C = \overline{V}_s\big|_{\overline{z}=0} = \frac{\rho_l}{\rho_s}\frac{\vec{V}_g}{V_0} \tag{11}$$

$$\theta_C = \theta_s\big|_{\overline{z}=0} = 0 \tag{12}$$

$$\nabla \overline{C}_C = 0 \tag{13}$$

Along the outside ampoule wall:

$$\theta_w = \theta_w(\overline{z}) = \begin{cases} \theta_C, & 0 < \overline{z} < \overline{z}_1 \\ \theta_C + TGH^*(\overline{z} - \overline{z}_1), & \overline{z}_1 < \overline{z} < \overline{z}_2 \\ \theta_C + TGH^*(\overline{z}_2 - \overline{z}_1) + TGL^*(\overline{z} - \overline{z}_2), & \overline{z}_2 < \overline{z} < \frac{L}{R} \end{cases} \tag{14}$$

Where, $\overline{z}_1$ and $\overline{z}_2$ are the lower and upper limits of the steep gradient zone respectively. TGH and TGL are temperature gradients in the steep and shallow gradient zones respectively.

In both liquid and solid sides along the inner wall:

$$\theta_w = \theta_l \tag{15}$$

$$\vec{n} \cdot \frac{\overline{\overline{k}}_w}{k_l} \cdot \nabla \theta_w = \vec{n} \cdot \nabla \theta_l \tag{16}$$

$$\theta_w = \theta_S \tag{17}$$

$$\vec{n} \cdot \frac{\overline{\overline{k}}_w}{k_s} \cdot \nabla \theta_w = \vec{n} \cdot \nabla \theta_s \tag{18}$$

$$\overline{V} = \frac{\vec{V}_g}{V_0} \tag{19}$$

$$\nabla \overline{C} \cdot \vec{n}_r = 0 \tag{20}$$

where $\overline{\overline{k}}_w$ is a tensor and is defined in Table 1. Along the symmetry central line, i.e., at $r = 0$ for both liquid and solid phases:

$$\overline{V} \cdot \vec{n}_r = 0 \tag{21}$$

$$\nabla \theta \cdot \vec{n}_r = 0 \tag{22}$$

$$\nabla \overline{C} \cdot \vec{n}_r = 0 \tag{23}$$

Along the liquid-solid interface, i.e., at $\overline{z} = S/R$:

$$\theta_s = \theta_l = \theta_m \tag{24}$$

$$\frac{1}{Ma_T} \nabla \theta_l \cdot \vec{n} - \frac{k_s}{k_l} \frac{1}{Ma_T} \nabla \theta_s \cdot \vec{n} = \frac{\rho_s}{\rho_l} \frac{1}{St} (\overline{V}_s - \overline{V}_l) \cdot \vec{n} \tag{25}$$

$$(\overline{V}_l - \overline{V}_m) \cdot \vec{n} = \frac{\rho_s}{\rho_l} (\overline{V}_s - \overline{V}_m) \cdot \vec{n} \tag{26}$$

$$(\overline{V}_l - \overline{V}_s) \cdot \vec{t} = 0 \tag{27}$$

$$\frac{\rho_s}{\rho_l} \overline{C}_s (\overline{V}_s - \overline{V}_m) \cdot \vec{n} - \overline{C}_l (\overline{V}_l - \overline{V}_m) \cdot \vec{n} = \frac{1}{Ma_S} \nabla \overline{C}_l \cdot \vec{n} - \frac{\rho_s}{\rho_l} \frac{D_s}{D_l} \frac{1}{Ma_S} \nabla \overline{C}_s \cdot \vec{n} \tag{28}$$

$$\overline{C}_s = \kappa \overline{C}_l \tag{29}$$

Where unit normal n points from the liquid into the solid and κ is the partition coefficient.

Adiabatic and impermeable boundary conditions are applied along the bubble's free surface, i.e.,

$$\nabla \theta \cdot \vec{n} = 0 \tag{30}$$

$$\nabla \overline{C} \cdot \vec{n} = 0 \tag{31}$$

and the stress balance conditions on the bubble surface are:

$$\overline{\sigma}_n = 2We^{-1} \overline{H} - \overline{P}_a \tag{32}$$

$$\overline{\sigma}_t = \nabla \overline{\gamma} \cdot \vec{t} \tag{33}$$

Where $\overline{\sigma}_n = \frac{\sigma_n}{\sigma_o}$, $\sigma_o = \rho V_o^2$, $\overline{P}_a = \frac{P}{P_o}$, $P_o = \rho V_o^2$, $\overline{H} = HR$, $\overline{\sigma}_t = \frac{\sigma_t}{\sigma_o}$, $\overline{\gamma} = \frac{\gamma}{\gamma_o}$ and $\gamma_o = \rho V_o^2 R$

Eq. (33) describes the driving force for the thermocapillary convection generated at the bubble surface due to the temperature dependence of the surface tension and couples the momentum and energy equations. Because the surface tension coefficient is negative, the fluid will flow from the higher temperature region to lower temperature region.

The thermophysical properties of GaAs and the different dimensionless parameters that appear in the governing equations and boundary conditions together with their nominal values as used in the present analysis are listed in Table 1 and summarized in Table 2. This table indicates that the solutal Marangoni number is quite high. Therefore, the transport of species in the melt as described by Equation (4) is dominated by convection rather than diffusion.

3 Numerical Methodology

The problem is solved numerically using a customized version of the finite element code FIDAP. In the model, the shapes of the growth interface and the bubble interface are not known a priori. Consequently, both the solid-melt and bubble-melt interfaces should be modeled as moving boundaries that are updated at each step.

In general, the balance of normal and tangential stresses along the bubble-wall interface can be used to satisfy the boundary conditions in the momentum equation and the kinematic constraint is used to update the location of the free surface. However, to shorten the computational times, the present analysis is simplified by fixing the shape of the bubble, as well as its location in the melt. Therefore, the simulations presented here can be regarded as snapshots in time as the solidification process proceeds.

The shape and position of the bubble are fixed by setting the normal velocities of the nodes on the surface of the bubble and at the bubble tips to be zero and by fixing the contact angle between the bubble and either the line of symmetry or the ampoule wall (depending on whether the bubble is located along the central axis or along the side wall respectively). For the present phase change problem, the balance of energy flux across the growth interface, as in Equation (25), is used to update the position of the nodes on the solid-liquid interface.

The solution is obtained in two steps. In the first step, the global system of equations for continuity, energy, and momentum is solved in a pseudo-transient manner by marching out in time to a steady state solution using a first order backward Euler integration scheme. At each time step, the continuity, energy, and momentum equations are solved sequentially using a segregated Gaussian elimination solver. The pseudo-transient solutions were obtained by starting from a field in conductive equilibrium subjected to a uniform pulling velocity with an initially planar interface. Since solutal buoyancy and solutal dependencies on the melting temperature are negligible, the species conservation equation is completely decoupled from the energy and momentum equations. Therefore, in the second step, the conservation equation for the solute can be solved separate from the other conservation equations. The species equation is obtained using Gaussian elimination with solutions of velocity, temperature, interface shape, and mesh geometry generated in the first step as input to the steady state solver.

To arrive at a converged solution, two convergence criteria must be satisfied simultaneously. These criteria are:

$$\left\| \frac{S_i - S_{i-1}}{S_i} \right\| \leq \varepsilon_S \tag{34}$$

$$\left\| \frac{R_i}{R_o} \right\| \leq \varepsilon_R \tag{35}$$

where S_i and R_i are respectively the solution and residual force vectors at iteration i. The norm $||\quad||$ is the root-mean-square norm summed over all of the equations. For both criteria, the tolerances, ε_S and ε_R, were set to 0.0001. In addition to the above two criteria, when solving for the position of the growth interface, an additional convergence criteria is needed:

$$\|\delta_i\| \leq \varepsilon_\delta \tag{36}$$

Where $\|\delta_i\|$ is the norm of the free surface deflection at iteration i. In the present model, the tolerance for surface deformation is also specified to be 0.0001. Our numerical experiments indicate that a combination of these three tolerances provides an effective overall convergence criterion for most situations.

To give an indication of the convergence behavior of the solution method, when the bubble is located on the sidewall at l=4.56 cm, a steady-state was achieved in the first step after marching out approximately 10,000 seconds. The species equation converged after 26 iterations for this bubble configuration.

Comprehensive grid convergence tests are performed for both bubble-in-center and bubble-on-wall configurations. Comparisons are made on the basis of the following variables: maximum velocity, $V_{\max}$; maximum absolute stream function value, $|\psi|_{\max}$; maximum concentration, $C_{\max}$; solutal segregation, $(C_{max}\text{-}C_{min})/C_0$; and the maximum interface deflection, $\delta_{\max}$. Two bubble locations are chosen. One is at l=4.56 cm, where the bubble is located at the shallow temperature gradient (dT_h/dz =0.34783$^\circ C/cm$). Another is at l=0.5cm, where the bubble is located at the steep temperature gradient (dT/dz =15$^\circ C/cm$). The bubble radius is fixed at 0.24cm. The results for the bubble-in-center and bubble-on-wall configuration are included in Tables 3 and 4, respectively.

Based on these results, the 1861 element mesh (the finest grid) was chosen for generation of the parametric results. The numbers in parenthesis represent the percentage difference between the current mesh and the finest mesh. Spot checking of the solutions for special cases proved very little improvement in the results as the node number increases beyond this "finest mesh".

4 Results and Discussion

In the present numerical study, four different bubble sizes and two different configurations are considered. The two

Table 1 : Thermophysical Properties and Experimental Parameters for GaAs Bridgman Growth

Parameter	Symbol	Value
Ampoule Length	L_A	16.5 cm
Length of Steep Gradient Zone	L_g	2 cm
Sample Radius	R_A	0.75 cm
Ampoule Inner Wall Thickness	δ	0.09 cm
Ampoule conductivity	$\overline{\overline{k}}_w$	$\begin{bmatrix} 0.1434 & 0 \\ 0 & 0.01195 \end{bmatrix}$ cal/s-cm-°C
Density of Boron Nitride	ρ_{wl}	2.15 g/cm^3
Bubble Radius	R	0.14 cm,0.24 cm, 0.34 cm, 0.44 cm
Interface Thermal Gradient	dT/dZ	15 °C / cm
Hot Zone Temperature Gradient	dT_h/dZ	0.34783 °C / cm
Cold Zone Temperature	T_c	1223 °C
Melting Temperature	T_m	1238 °C
Growth Velocity	V_g	2.5E-4 cm/s
Liquid Density	ρ_l	5.72 g/cm^3
Liquid Dynamic Viscosity	μ_l	0.042 g/cm-s
Liquid Conductivity	k_l	0.0425 cal/s-cm-°C
Liquid Specific Heat Capacity	c_{pl}	0.104 cal/g-°C
Liquid Thermal Expansion	β_t	1.87E-4 °C
Liquid Species Diffusivity	D_l	2E-5 cm^2/s
Interface Surface Tension	γ	1670-0.96 T dyne/cm
Interface Surface Tension Gradient	γ_T	-0.96 dyne/cm-°C
Latent Heat	L	173.7 cal/g
Solid Density	ρ_s	5.16 g/cm^3
Solid Conductivity	k_s	0.017 cal/s-cm-°C
Solid Specific Heat Capacity	c_{ps}	0.10 cal/g-°C
Solid Species Diffusivity	D_s	2E-9 cm^2/s
Partition coefficient	κ	0.1

Table 2 : Dimensionless Parameters

PARAMETER	DEFINITION	VALUE
Reynolds No.	$Re = \frac{U_o R}{\nu}$	21∼9040
Prandtl No.	$\mathrm{Pr} = \frac{\nu}{\alpha}$	0.103
Schmidt No.	$Sc = \frac{\nu}{D}$	367
Thermal Marangoni No.	$Ma_T = Re \cdot \mathrm{Pr}$	2.163∼931
Solutal Marangoni No.	$Ma_S = Re \cdot Sc$	7.7E3∼3.3E6
Grashof No.	$Gr = \frac{g\beta_t \Delta T R^3}{\nu^2}$	3E-4∼1E-2
Capillary No.	$Ca = \frac{\mu U_o}{\gamma}$	9.7E-5∼1.32E-2
Stefan No.	$St = \frac{c_{pl}\Delta T}{L}$	0.02
Weber No.	$We = Re \cdot Ca$	2E-3∼119
Dimensionless Body Force	$F_b = \frac{\rho_l g R^2}{V_o \mu}$	1.14E-6∼2.1E-3

configurations correspond to a spherical bubble in the center of the ampoule and an annular bubble attached to the ampoule wall as shown schematically in Figs. 3a and 3b, respectively. For each configuration the bubble radii are varied between 0.14 cm and 0.44 cm. In each of the case studies presented here, the position and shape of the

Table 3 : Grid-Independent Checks for Void-in-Center Configuration.

Distance between bubble and interface	Number of Elements	$V_{\max}$ (cm/s)	$\lvert\psi\rvert_{\max}$ (cm^2/s)	$C_{\max}$	$\frac{(C_{\max}-C_{\min})}{C_0}$	$\delta_{\max}$ (cm)
$l = 4.56$ cm	1735	0.5427	0.05750	5.71476092	3.11154252	0.2928547
	1371	0.5636 (3.85)	0.05752 (3.48)	5.6992 (0.27)	3.28024772 (5.42)	0.29610236 (1.11)
	959	0.5675 (4.57)	0.0542 (5.75)	5.6832 (0.55)	3.33552552 (7.2)	0.29765985 (1.64)
$l = 0.5$ cm	1861	5.51	0.37356	1.61917729	0.34111833	0.79064861
	1343	5.493 (0.31)	0.36469 (2.37)	1.4209 (12.25)	0.30370173 (10.97)	0.81003154 (2.45)
	886	5.56 (0.91)	0.359 (3.90)	1.3608 (15.96)	0.25280535 (25.89)	0.81136497 (2.62)

Table 4 : Grid-Independent Checks for Void-on-Wall Configuration.

Distance between bubble and interface	Number of Elements	$V_{\max}$ (cm/s)	$\lvert\psi\rvert_{\max}$ (cm^2/s)	$C_{\max}$	$\frac{(C_{\max}-C_{\min})}{C_0}$	$\delta_{\max}$ (cm)
$l = 4.56$ cm	1757	0.7724	0.11656	5.71590326	3.10649979	0.29287699
	1393	0.7769 (0.58)	0.11561 (0.82)	5.7063 (0.17)	3.27836839 (5.53)	0.29603647 (1.08)
	987	0.8493 (9.96)	0.11557 (0.85)	5.692 (0.42)	3.33559877 (7.37)	0.29744201 (1.56)
$l = 0.5$ cm	1799	7.261	1.4115	1.3828	0.12443623	0.32849842
	1365	7.307 (0.64)	1.3978 (0.97)	1.367 (1.14)	0.12087964 (2.86)	0.33345414 (1.51)
	920	7.456 (2.69)	1.3845 (1.92)	1.3394 (3.14)	0.14503224 (16.55)	0.31974799 (2.66)

bubble are fixed and the flow, temperature and concentration fields in the growth ampoule are obtained through quasi-steady numerical simulations that can be regarded as snapshots in time as the crystal growth process takes place in the ampoule at very slow growth rates.

4.1 Flow and Concentration Fields

The flow and concentration fields for the bubble-in-center configuration with l fixed at 4.56 cm is shown in Fig. 4 for three different bubble sizes. In this case, as evident from the streamline pattern around the bubble, relatively strong thermocapillary convection is generated due to the interfacial tension that carries the warm fluid downwards along the interface into the lower regions of the ampoule. Consequently, counter-rotating vortices are generated in the melt near the bubble. However, the vortices are not sufficiently strong and large to affect the growth front for any of the bubble radii considered.

This is confirmed by an examination of the concentration fields in Fig. 4 where it is evident that the thermocapillary vortices have not yet penetrated into the solutal build-up layer next to the growth front. The segregation pattern in this case is caused by diffusion of solute in the normal direction emanating from the slightly parabolic interface. This naturally creates an accumulation of species in the center of the ampoule very close to the growth front. In this case, the thermal field near the growth interface is also not noticeably affected by the thermocapillary convection and the slight parabolic shape of the growth interface in this case as indicated in

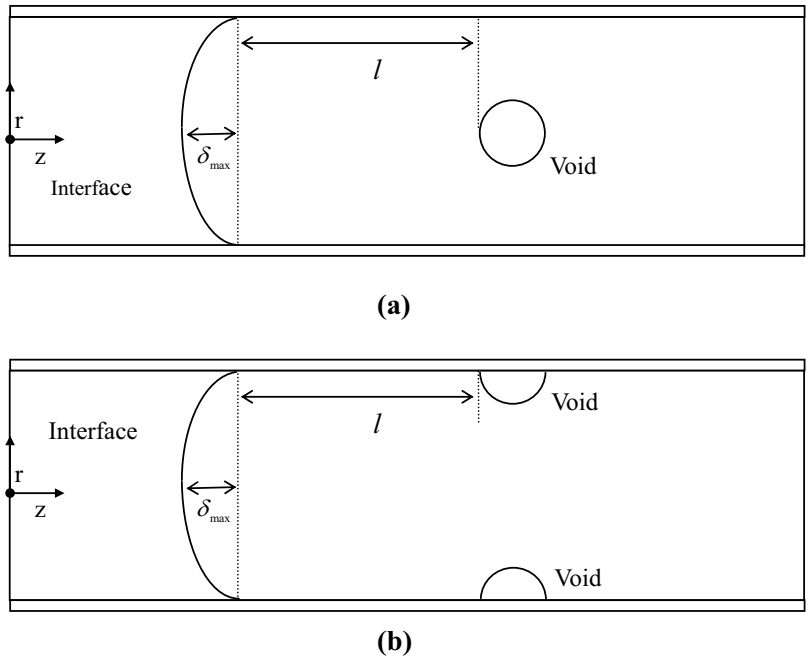

Figure 3 : Sketch of (a) Bubble-in-Center Configuration; (b) Bubble-on-Wall Configuration

Fig. 4 is mainly due to a mismatch among the thermal conductivities of the solid, melt and the ampoule.

The situation changes when the growth interface is at l= 1.95 cm away from the bubble as shown in Fig. 5. In this case, the thermocapillary vortices can penetrate the solutal build-up layer for the two larger bubble sizes and, as evident from the concentration contours near the growth interface, the diffusion-dominated solutal layer near the growth front is nearly wiped out as the vortices carry the solute from the center of the ampoule to the sidewall. In this case, the interface shape remains unaffected by the thermocapillary convection as conduction is still the dominant mode of heat transfer in the low Prandtl number melt.

When the growth interface gets very close to the bubble, as in l = 0.5 cm, the growth conditions are drastically modified. This is true even for the smallest bubble size as shown in Fig. 6. In this case, the bubbles are mostly in the high temperature gradient zone of the furnace and the resulting thermocapillary convection is quite intense. As a result, the solutal layer is completely destroyed by the bubble-generated convection for all the bubble sizes. The temperature field is also drastically affected by the higher levels of convection and results in a more curved solid-liquid interface. Our numerical results shown in Fig. 6 indicate that for the largest bubble radius of 0.44 cm, although the growth interface is drastically stretched and curved due to the modification of the thermal field by thermocapillary convection, the solutal concentration at the growth front is quite uniform due to the intense mixing action of the recirculating vortices.

The bubble-on-wall results are depicted in Figs. 7-9. Examination of these figures point to 4 marked differences between the bubble-in-center and bubble-on-wall results. First, the two main thermocapillary vortices in the bubble-on-wall case rotate in the opposite direction to the bubble-in-center case and are noticeably weaker in intensity due to the dampening effect of the walls. Second, as a result of the lower intensity and limited extent of the vortices, the thermocapillary convection does not begin to affect the solutal layer near the growth interface until the bubble is within l = 1.5 cm of the growth front, a delay of 0.45 cm compared to the bubble-in-center case. Third, there is a pair of secondary vortices in the bubble-on-wall case that become quite noticeable when the bubble is in the shallow gradient region of the furnace, especially, for the larger radii of 0.34 cm and 0.44 cm as indicated in Fig. 7. This is due to a change in the sign of the interfacial temperature gradient as the bubble interface temperature goes through a local minimum for the bubble-on-wall case as shown in Fig. 9 for the two dif-

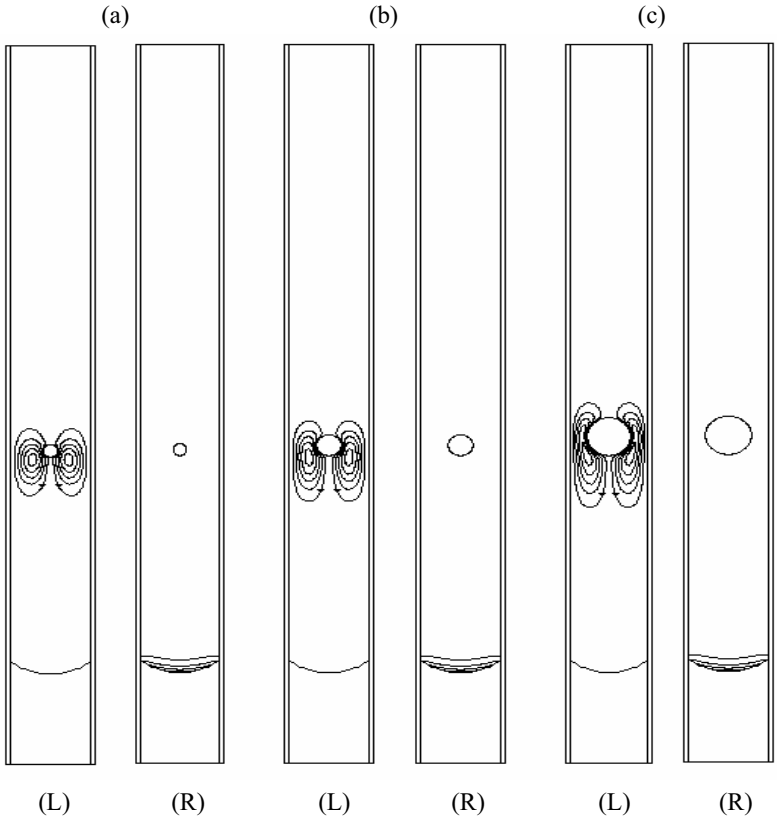

Figure 4 : Streamlines (L) and Isoconcentration Lines (R) for Three Different Sizes of Bubble, Bubble-in-Center Configurations at l=4.56cm: (a) $r = 0.14cm$ [5 contours, $\Psi_{max} = 0$, Ψ_{min} =-0.027259; C_{max} =5.7149, C_{min} =0]; (b) $r = 0.24cm$ [5 contours,Ψ_{max} =0,Ψ_{min} =-0.057503;C_{max} =5.7148, C_{min} =0]; (c)$r = 0.44cm$[5 contours, Ψ_{max} =0, Ψ_{min} =-0.08741; C_{max} =5.7146, C_{min} =0]

ferent locations of l= 1.5 cm and l= 0.5 cm. At l= 1.5 cm, the bubble interface is in the shallow furnace temperature gradient region and the local minimum occurs at a position of around 0.35 cm along the bubble interface, while at l= 0.5 cm the bubble is mostly contained in the high furnace temperature gradient region and the local minimum occurs at a position of around 0.10 cm along the bubble interface. Consequently, in the former case, the secondary vortices are less disturbed by the presence of the wall and the interface and can thus grow to a larger extent than in the latter case. This is also confirmed by the numerical simulations where for the 0.44 cm bubble, the secondary vortices are more prominent in Fig. 7 for the l= 1.5 cm case than when they are closer to the growth interface at l=0.5 cm as in Fig. 8. Finally, the fourth main difference between the bubble-on-wall and bubble-in-center case is with regard to the effect of the bubble on the growth interface shape. In the bubble-on-wall case the growth interface shape is still affected by the bubble-generated flow when the growth interface is close to the bubble as in Fig. 8. But due to the lower intensity of the flow, the extent of the interfacial curvature and stretching is not as drastic as the bubble-in-center case. Notwithstanding these differences when the growth interface gets sufficiently close to the bubble (in this case below l= 1.5 cm), the mixing provided by the bubble-generated convection renders a well-mixed growth condition at the phase front.

4.2 Dopant Concentration along the Growth Interface

The effect of bubble-generated convection on the interfacial dopant concentration is shown in Figs. 10 and 11 for the bubble-in-center and bubble-on-wall configurations respectively. Profile-1 on these figures corresponds to the situation where the thermocapillary vortex is still too far to affect the growth conditions. As a result, a domed

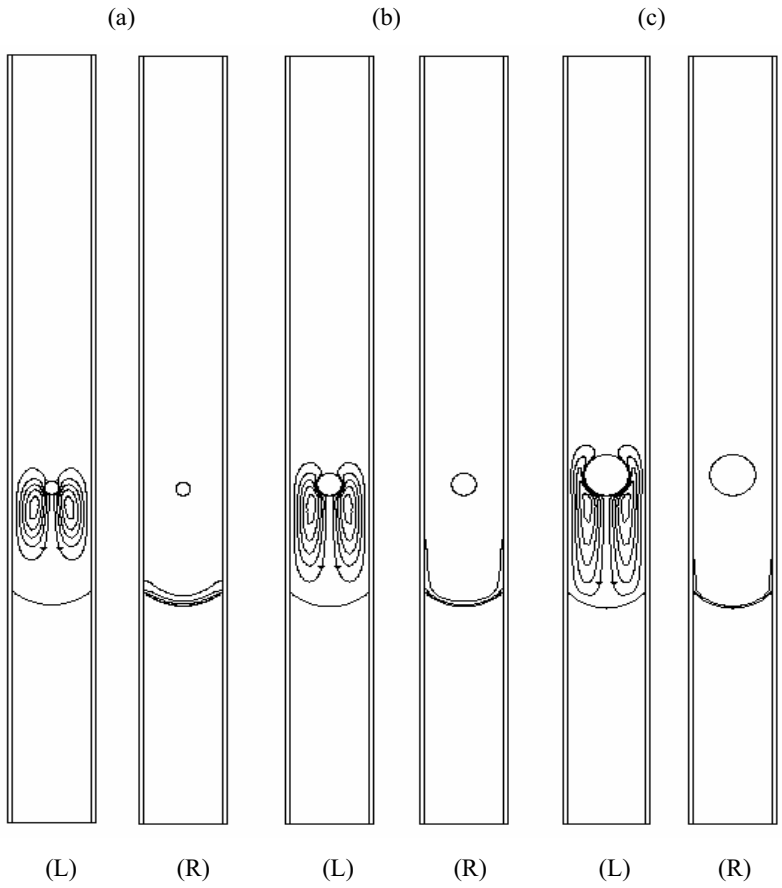

Figure 5 : Streamlines (L) and Isoconcentration Lines (R) for Three Different Sizes of Bubble, Bubble-in-Center Configurations at l=1.95cm: (a) $r = 0.14cm$ [5 contours, Ψ_{max} =0, Ψ_{min} =-0.060799; C_{max} =4.3492, C_{min} =0]; (b) $r = 0.24cm$ [5 contours, Ψ_{max} =0, Ψ_{min} =-0.10671; C_{max} =2.6945, C_{min} =0]; (c) $r = 0.44cm$ [5 contours, Ψ_{max} =0, Ψ_{min} =-0.17238; C_{max} =1.8487, C_{min} =0].

dopant concentration profile is attained due to diffusion and accumulation of the rejected solute near the center of the growth interface. Profile-2 corresponds to the situation where upon the bubble-generated convection has just penetrated the solutal layer. The net effect of the primary thermocapillary vortices of the bubble-in-center case (see Fig. 5c) and the secondary vortices of bubble-on-wall case (see Fig. 7c) is the flattening of the profile near the center of the growth interface and slight to moderate accumulation of solute near the ampoule wall. Finally, Profile-3 in these figures corresponds to the situation where the solute build-up is completely wiped out by bubble-generated convection.

4.3 Radial Segregation

In order to describe the nature of the solutal segregation caused by the bubble-generated convection, the radial segregation is plotted against the distance between the bubble and the growth interface in Figs. 12a and 12b for the bubble-in-center and bubble-on-wall configurations respectively. Three distinct segregation regimes or regions are observed. The first region (extending roughly between l = 3.5-5.0 cm for bubble-in-center, and l= 2.0-5.0 cm for bubble-on-wall) corresponds to a diffusion controlled regime where segregation is mainly due to interfacial curvature. The second region (extending roughly between l=1.5-3.5 cm for bubble-in-center, and l=1.0-2.0 cm for bubble-on-wall configurations) corresponds to a transport regime where solutal segregation is governed by both diffusion and bubble generated convection. Finally, the third region (extending below l=1.5 cm for bubble-in-center, and l=1.0 cm for bubble-on-wall configurations) relates to a well-mixed regime where solutal concentration is completely uniform due to the mix-

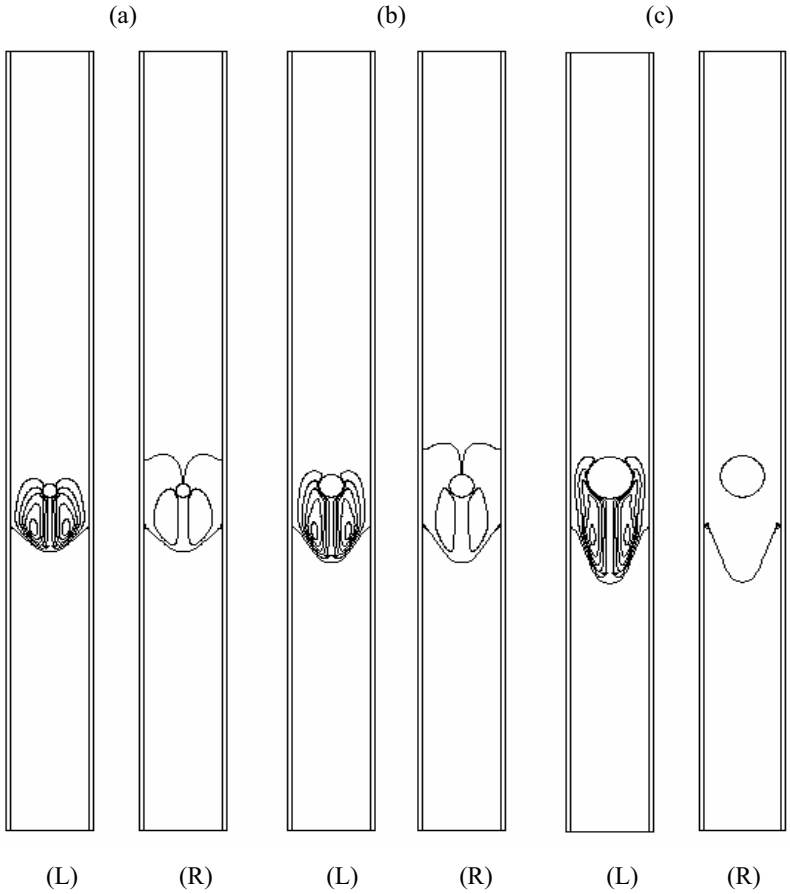

Figure 6 : Streamlines (L) and Isoconcentration Lines (R) for Three Different Sizes of Bubble, Bubble-in-Center configuration at l=0.5cm: (a) $r = 0.14cm$ [5 contours, Ψ_{max} =0, Ψ_{min} =-0.19255; C_{max} =1.8144, C_{min} =0]; (b) $r = 0.24cm$ [5 contours, Ψ_{max} =0, Ψ_{min} =-0.37356; C_{max} =1.6192, C_{min} =0]; (c) $r = 0.44cm$ [5 contours, Ψ_{max} =0.0017559,Ψ_{min} =-0.74269; C_{max} =1.3221,C_{min} =0]

ing provided by the bubble-generated convection.

Figs.13a and 13b display the dependence of radial segregation on the bubble size for the two configurations. It is clearly evident that in both the well-mixed and the diffusion dominated regimes bubble size plays a minor role while the extent of segregation is a strong function of the bubble radius in the transitionary region. Here radial segregation decreases at a diminishing rate with bubble size for the bubble-in-center case while it decreases at an increasing rate with bubble size for the bubble-on-wall configuration. This is attributed to the viscous dampening of the flow by the wall in the bubble-on-wall case that requires the bubble to be beyond a certain critical size before it can affect the interfacial conditions.

4.4 Interfacial Curvature

The effect of bubble-generated convection on the growth interface shape is displayed in Figs. 14 and 15. The maximum growth interface deflection is plotted as a function of the distance between the bubble and the growth interface in Figs. 14a and 14b for the bubble-in-center and bubble-on-wall configurations, respectively. From Fig. 14a, it is apparent that for the bubble-in-center case, beyond a distance of l_{crit} = 2.5 cm, the growth interface shape is relatively unaffected by bubble-generated convection for any bubble size. This critical distance seems to decrease to almost l_{crit} = 1.5 cm for the bubble-on-wall configuration as indicated in Fig. 14b. A closer examination of the effect of bubble size on growth interface curvature, for the bubble-in-center case as shown in Fig. 15a, reveals that the maximum growth interface deflec-

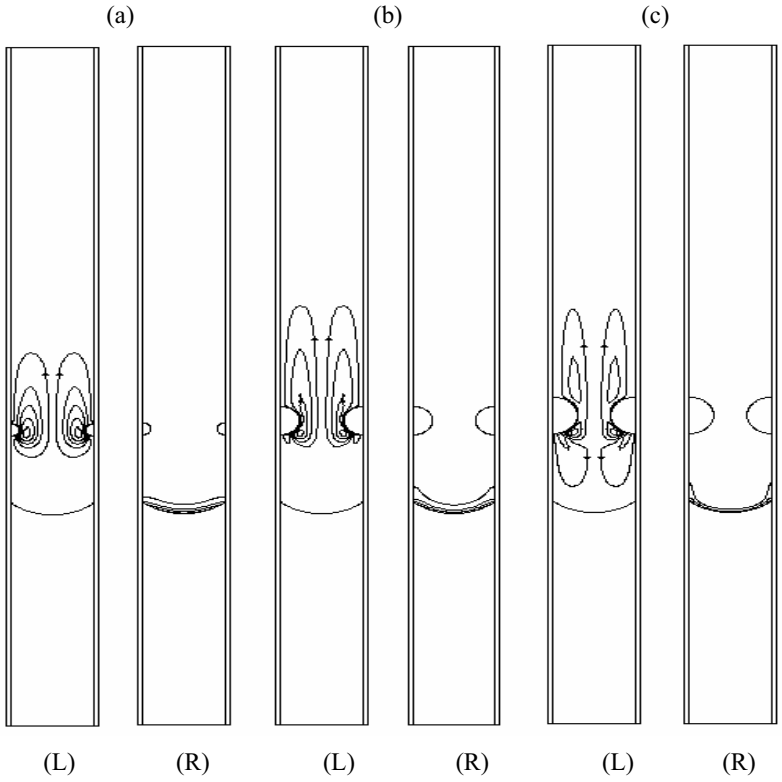

Figure 7 : Streamlines (L) and Isoconcentration Lines (R) for Three Different Sizes of Bubble, Bubble-on-Wall Configuration at l=1.5cm: (a) $r = 0.14cm$ [5 contours, Ψ_{max} =0.36423,Ψ_{min} =-0.026524;C_{max} =4.9974,C_{min} =0]; (b) $r = 0.34cm$ [5 contours,Ψ_{max} =0.36538,Ψ_{min} =-0.11304; C_{max} =3.923, C_{min} =0]; (c) $r = 0.44cm$ [5 contours, Ψ_{max} =0.30184,Ψ_{min} =-0.14726; C_{max} =2.3371, C_{min} =0]

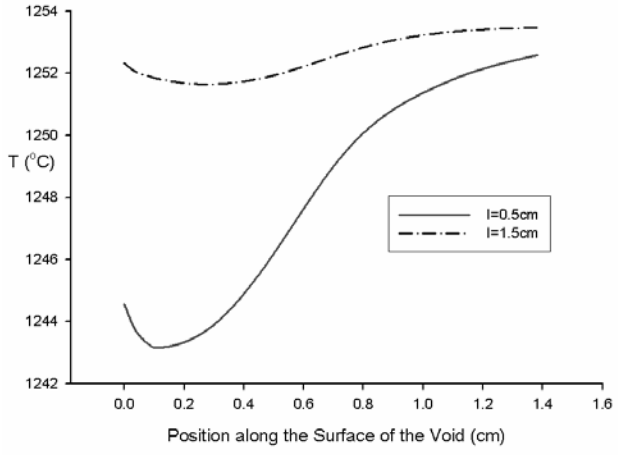

Figure 9 : Temperature Profile along The Bubble Surface with The Bubble in The Steep Gradient Zone (Bubble-on-Wall Configuration)

tion is almost linearly dependant on the bubble radius. However, for the bubble-on-wall configuration, the maximum growth interface deflection decays to a constant value below the critical radius of 0.34 cm as shown in Fig. 15b. Again this is attributed to the fact that for the bubble-on-wall case, the bubble has to be above a critical radius before it can impact the interfacial conditions.

5 Conclusions

An axi-symmetric quasi-steady numerical analysis was performed to investigate the effects of bubble-driven convection on the solidification of a binary dilute alloy in microgravity. Attention was particularly focused on the effect of the bubble size and the distance between the bubble and the growth interface on the growth interface shape and the radial segregation patterns. Through parametric numerical simulations, three different growth regimes were identified based on the distance between the bubble and the growth interface. According to this

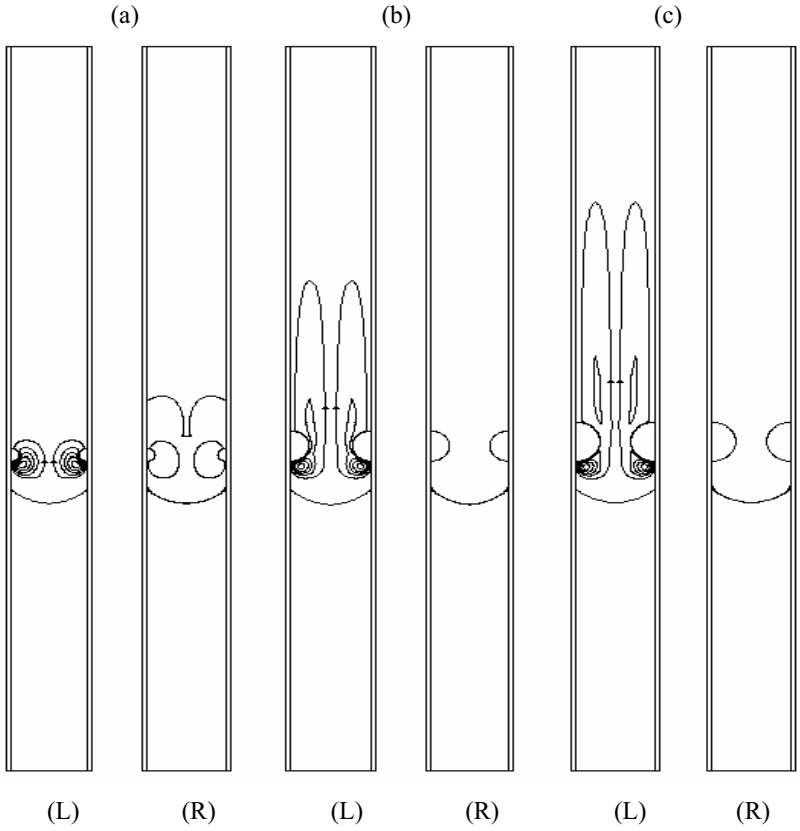

Figure 8 : Streamlines (L) and Isoconcentration Lines (R) for Three Different Sizes of Bubble, Bubble-on-Wall Configurations at l=0.5cm: (a) $r = 0.14cm$ [5 contours, Ψ_{max} =1.1563, Ψ_{min} =-0.045955; C_{max} =1.6047, C_{min} =0]; (b) $r = 0.34cm$ [5 contours,Ψ_{max} =1.4525,Ψ_{min} =-0.093672; C_{max} =1.2997,C_{min} =0]; (c) $r = 0.44cm$ [5 contours, Ψ_{max} =1.3327,Ψ_{min} =-0.068849; C_{max} =1.3166, C_{min} =0]

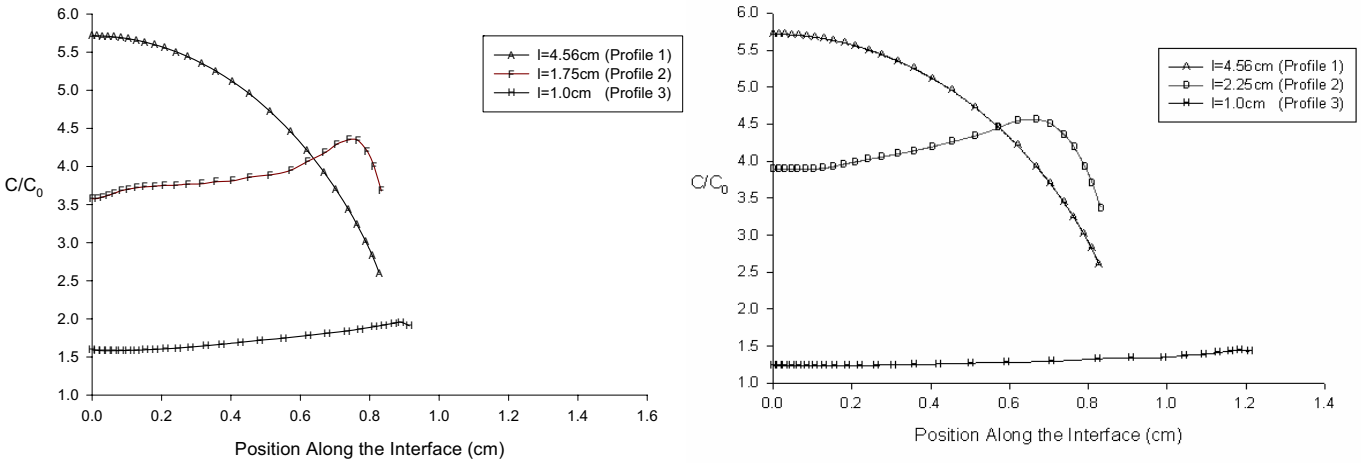

(a) (b)

Figure 10 : Dopant Concentration along the Growth interface for the Bubble-in-Center Configuration, (a) Bubble Radius=0.14 cm; (b) Bubble Radius=0.34 cm.

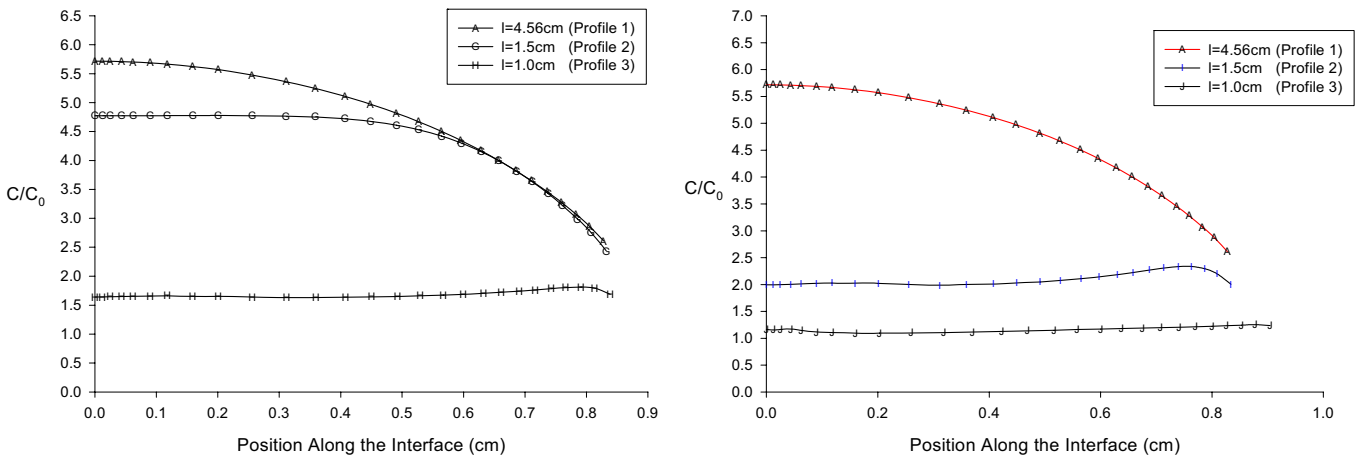

Figure 11 : Dopant Concentration along the Growth interface for The Bubble-on-Wall Configuration, (a) Bubble Radius=0.24 cm; (b) Bubble radius=0.44cm.

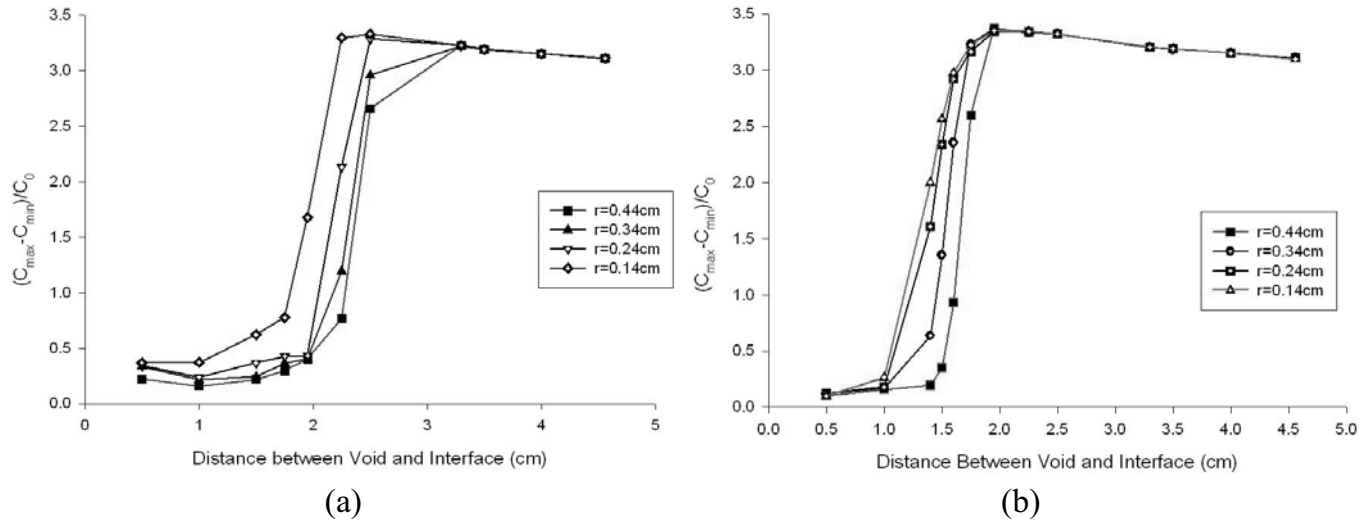

Figure 12 : Radial Segregation as a Function of the Distance between the Bubble and the Growth Interface for (a) Bubble-in-Center Configuration; (b) Bubble-on-Wall Configuration

designation, when the bubble is relatively far from the growth interface, a diffusion-controlled regime prevails where most of the radial nonuniformity in the interfacial composition is due to interface curvature. In this regime, bubble size does not have a noticeable effect on the extent of radial segregation or the shape of the growing interface. When the bubble is relatively close to the growth interface, a fully-mixed regime prevails whereupon the solutal boundary layer is completely eliminated by the penetrating thermocapillary vortex and the interfacial composition is greatly homogenized. In this regime, bubble size, again, does not have a significant effect on the segregation profiles because even the smallest bubble considered generates sufficient mixing to homogenize the solute concentration at the growth interface. But bubble size can impact the growth interface shape noticeably, producing highly stretched interface curvatures for the larger bubbles. These two regimes are separated by an intermedi-

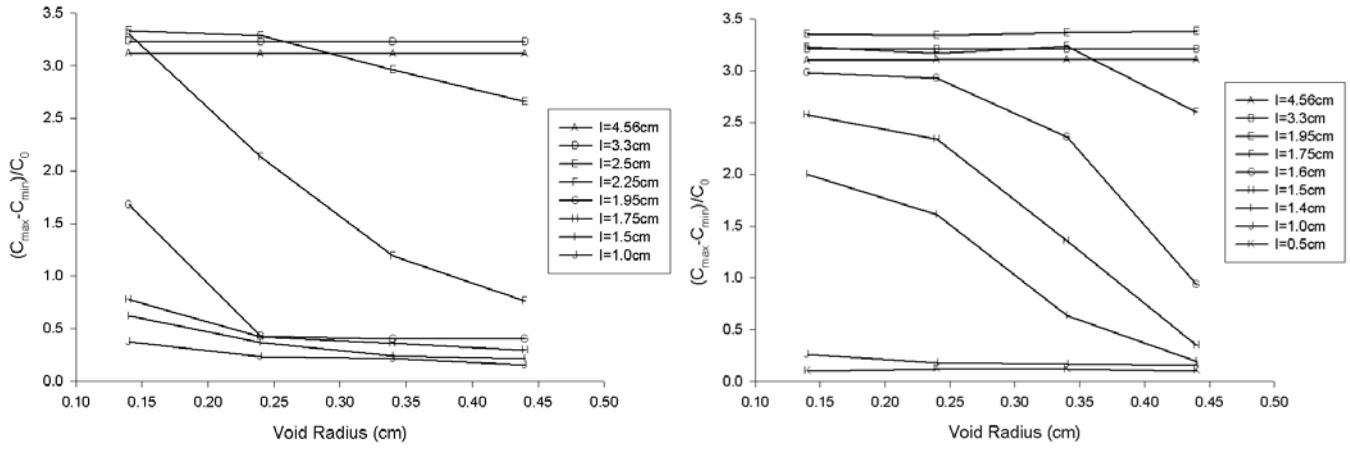

Figure 13 : Radial Segregation as a Function of Bubble Radius for (a) Bubble-in-Center Configuration; (b) Bubble-on-Wall Configuration.

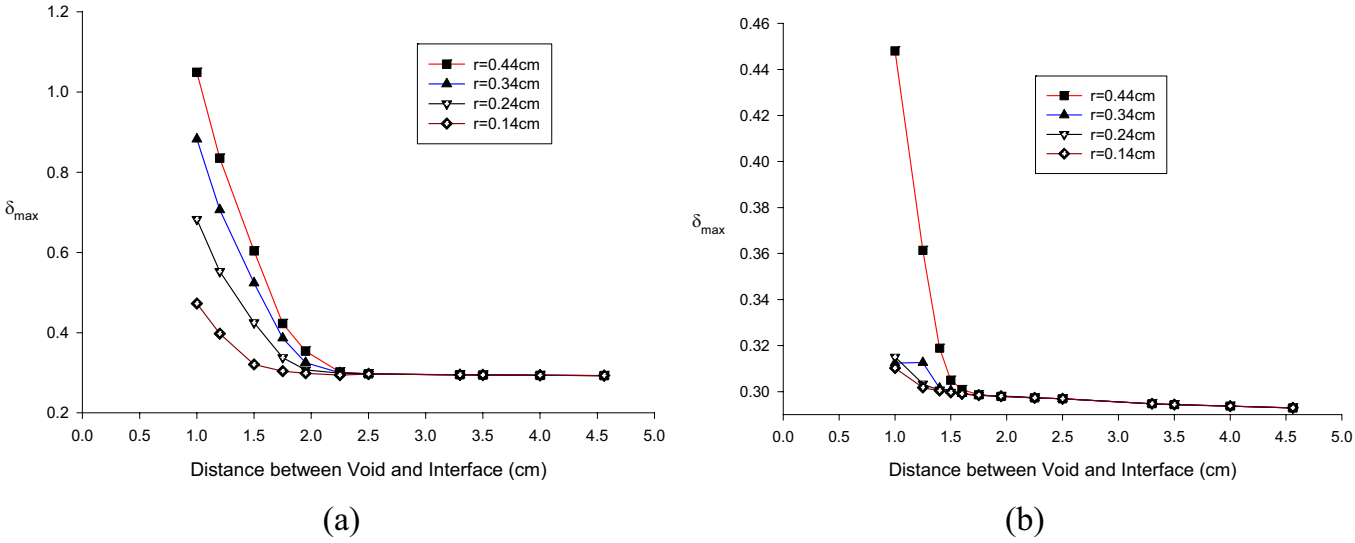

Figure 14 : Maximum Growth Interface Deflections as a Function of the Distance between the Bubble and the Growth Interface for (a) Bubble-in-Center Configuration; (b) Bubble-on-Wall Configuration

ate transitionary region where the radial interfacial concentrations change drastically with the distance between the bubble and the growth interface and are strong functions of bubble size. However, in this region the growth interface shape is only moderately affected by the bubble dimensions. Although the above-mentioned trends are common to both the bubble-in-center and the bubble-on-wall configurations, our numerical simulations indicate while the magnitudes of the radial segregations are mainly in the same range, the interfacial deflections and the parametric demarcation of the three regions are all noticeably different for the two bubble configurations.

Acknowledgement: Support from NASA HQ, Microgravity Physical Science Division is gratefully acknowledged.

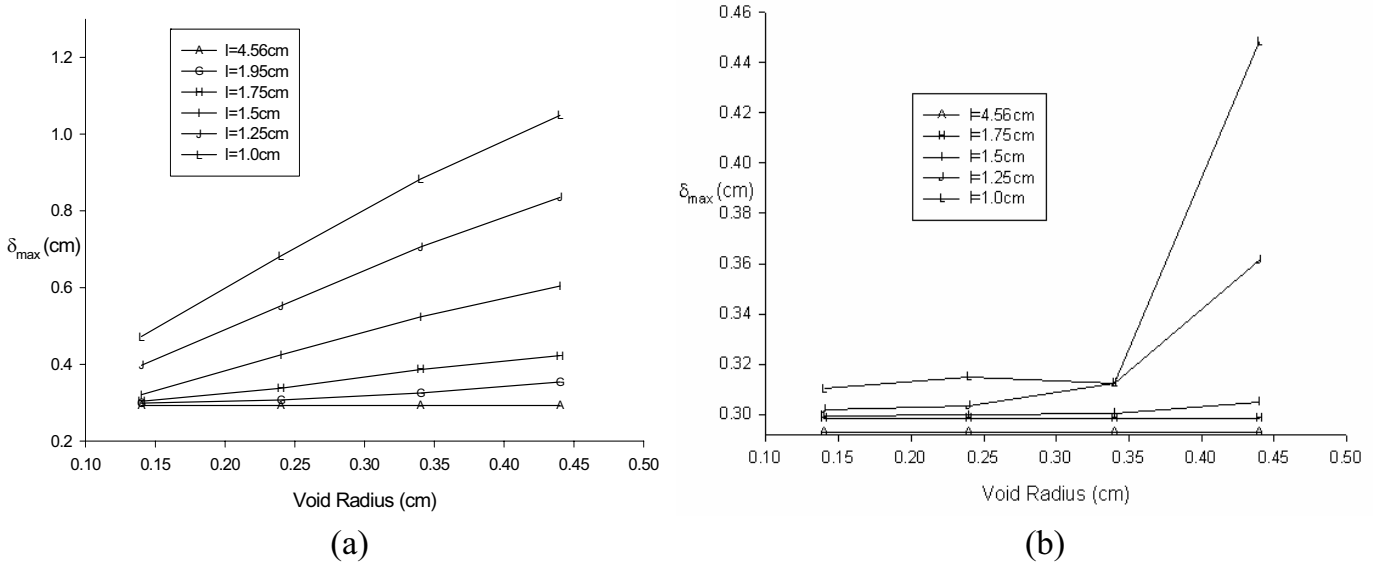

Figure 15 : Maximum Growth Interface Deflections as a Function of Bubble Radius for (a) Bubble-in-Center Configuration; (b) Bubble-on-Wall Configuration.

References

Andrews, J. B.; Hayes, L.J.; Arikawa, Y.; and, Coriell, S.R. (1997): Microgravity Solidification of AlIn Alloys, *AIAA Paper* 97 – 1012, *The 35th AIAA Aerospace Sciences* Meeting

Brown, R.A. (1988): Theory of Transport Processes in Single Crystal Growth from the Melt, *AIChE J.* vol.34 (6) pp.881-911.

Burton, J.A.; Prim, R.C.; Slichter, W.P. (1953): The Distribution of Solute in Crystals Grown from the Melt. Part I: Theoretical, *J. Chemical Physics*, vol. 21 (11), pp. 1987 – 1991.

Carruthers, J.R. (1977): Crystal Growth in a Low Gravity Environment, J. Crystal Growth, vol.42, pp. 379-385.

Coriell, S.R.; Sekerka, R.F. (1979): Lateral Solute Segregation During Unidirectional Solidification of a Binary Alloy with a Curved Solid-Liquid Interface, *J. Crystal Growth*, vol.46, pp. 479-482.

Crouch, R.K.; Fripp, A.L.; Debnam, W.J.; Clark, I.O.; Carlson, F.M. (1982): Ground Based Studies for the Space Processing of Lead Tin Telluride, in: G.E. Rindone (Ed.), *Materials Processing in the Reduced Gravity Environment of Space*, North-Holland, New York, pp. 611-618.

Esmaeeli A., (2005), "Phase Distribution of Bubbly Flows under Terrestrial and Microgravity Conditions", *FDMP: Fluid Dynamics & Materials Processing* Vol. 1, No.1 , pp. 63-80.

Fripp, A.L.; Debnam, W.J.; Woodell, G.A.; Rosch, W.R.; Narayanan, R. (1997): The Effect of Microgravity Direction on the Growth of PbSnTe, *AIAA Paper* 97 – 0676.

Kassemi, M.; Rashidnia, N. (1997a): Steady and Oscillatory Thermocapillary Flows Generated by a Bubble in 1-G and Low-G Environments, *AIAA Paper 97-0924*,The 35th AIAA Aerospace Sciences Meeting

Kassemi. M.; and Rashidnia, N. (1997b): Oscillatory and Steady Thermocapillary and Natural Convective Flows Generated by a Bubble: Numerical-Experimental Comparisons, *Proceedings of the Joint Xth European and Russian Symposium on Physical Sciences in Microgravity*, Eds V.S. Avdyevsky and V.I Polezhaev, vol I, pp. 110-117

Kassemi. M.; Rashidnia, N.; Mercer, C. (1998): Numerical and Experimental Visualization of Oscillatory Temperature and Velocity Fields Generated by a Bubble, *Proceedings of The 8th International Symposium in Flow Visualization*, Eds. G.M. Carlomagno and I. Grant, pp. 284.1-284.11

Kassemi, M; and Rashidnia, N. (2000) Steady and Oscillatory Thermocapillary Convection Generated by a

Bubble, *Physics of Fluids*, vol.12, no. 12, pp. 3133-3146.

Kassemi, M.; Barsi, S.; Kaforey, M.; Matthiesen, D. (2001a): Effect of Void Location on Segregation Patterns in Microgravity Solidification, *J. Crystal Growth,* vol.225, pp. 516-521.

Kassemi, M.; Kaforey, M.; Matthiesen, D. (2001b): Effect of Void Generated Thermocapillary Convection on Dopant Segregation in Microgravity Solidification, *J. Thermophysics and Heat* Transfer, vol. 15 (2), pp. 219-227.

Lappa M., (2005), "Coalescence and non-coalescence phenomena in multi-material problems and dispersed multiphase flows: Part 2, a critical review of CFD approaches", *FDMP: Fluid Dynamics & Materials Processing*, Vol. 1, No. 3, pp. 213-234.

Lappa M., (2005), "Coalescence and non-coalescence phenomena in multi-material problems and dispersed multiphase flows: Part 1, a critical review of theories ", *FDMP: Fluid Dynamics & Materials Processing*, Vol. 1, No. 3, pp. 201-212.

Lehoczky, S.L.; Szofran, F.R. (1982): Directional Solidification and Characterization of Hg1-xCdxTe Alloys, in: G.E. Rindone (Ed.), *Materials Processing in the Reduced Gravity Environment of Space*, North-Holland, New York, pp. 409-420.

Matthiesen, D.H.; Majewski, J.A. (1993): The Study of Dopant Segregation Behavior During the Growth of GaAs in Microgravity, Joint "L+1" Science Review for USML-1 and USMP-1 with the Microgravity Measurement Group

Naumann, R. (1995): Marangoni Convection Around Voids in Bridgman Growth, *Journal of Crystal Growth*, vol. 154, pp. 156-162.

Ostrach, S. (1982): Low-Gravity Fluid Flows, *Ann. Rev. Fluid Mech.*, vol. 14, pp. 313-345.

Papazian, J. M.; Wilcox, W. R. (1978): *Interaction of Bubbles with Solidification Interfaces*, AIAA Journal, vol. 16, pp. 447-451

Tiller, W.A.; Jackson; K.A.;Rutter, J.W.;Chalmers, B. (1953): The Redistribution of Solute Atoms During the Solidification of Metals, Acta Metallurgica, vol. 1, pp. 428-437.

Wagner, C. (1954): Theoretical Analysis of Diffusion of Solutes During the Solidification of Alloys, *J. Metals,* vol. 6, pp. 154-160.

Wozniak, G.; Wozniak, K.; Bergelt, H. (1996): On the Influence of Buoyancy on the Surface Tension Driven Flow around a Bubble on a Heated Wall, *Experiments in Fluids*, Vol. 21, pp. 181-186.